Mechanical properties of a hybrid auxetic metamaterial and metastructure system

Wenjiao Zhang[a*], Shuyuan Zhao[b], Rujie Sun[c], Fabrizio Scarpa[d], Jinwu Wang[a*]

[a] School of Engineering, Northeast Agricultural University, No. 600 Changjiang Road, Harbin 150030, China

[b] Center for Composite Materials and Structures, Harbin Institute of Technology, Harbin 150080, China

[c] Department of Materials, Department of Bioengineering and Institute of Biomedical Engineering, Imperial College London, Prince Consort Road, London SW7 2AZ, UK

[d] Bristol Composites Institute (ACCIS), University of Bristol, Bristol BS8 1TR, UK

Abstract

We propose in this work an innovative hybrid auxetic metamaterial with a centresymmetric unit cell and tessellation topology similar to the one provided by the missing ribs configuration. The tessellation proposed is applied to different core unit cells (star shape, cross-chiral shape with same dimensions and re-entrant). The effects of the geometric parameters of the cells on the in-plane mechanical properties of this hybrid auxetic metamaterial system are investigated via finite elements (FEM). Representative unit cells (RUCs) with optimal mechanical behaviors are identified; those configurations exhibit the larger negative Poisson's ratios and enhanced specific moduli. Designs related to two groups of auxetic metastructures with cylindric and cubic shapes are then developed based on the optimized RUCs along x and y directions. The equivalent mechanical performance of these metastructures under internal pressure is evaluated from a numerical standpoint. Auxetic cylindrical metastructures can be tailored by adjusting the number of the optimized RUCs along the circumferential and longitudinal directions, together with the geometric parameters of the optimized RUC itself. These hybrid auxetic metamaterials and metastructures provide the potential for multifunctional applications in biomechanics, flexible electronics and aerospace.

Keywords: Star, Missing rib, Hybrid metamaterial system, Auxetic metastructure, Mechanical properties

1. Introduction

Auxetic mechanical metamaterials are typical structural material systems possessing the counter intuitive mechanical property of a negative Poisson's ratio (NPR). NPR materials contract transversely under uniaxial compression and expand laterally when stretched along one direction. The concept of auxeticity at experimental scale was first introduced by Lakes [1] when he pioneered the manufacture of polyurethane open cell foams with a re-entrant cell shape. Auxeticity can be provided by the geometry of the materials system and its internal deformation

mechanisms. Over decades, significant focus has been placed on developing auxetic metamaterials due to their excellent shear stiffness, indentation resistance, good performance in terms of dissipating mechanical energy, acoustic absorption and synclastic curvature [2, 3]. These unique properties are expected to be used in designing supports and protective structures in a variety of potential industrial applications like aerospace, architecture, furniture, sensors, damping structures, biomedical and bioengineering [4-8]. According to their structural deformation models, auxetic metamaterials can be classified into: missing rib, rigid (or semi-rigid) rotation, re-entrant, chiral and elastic instability-driven [9]. Amongst those, the missing rib model has received relatively less attention until Smith et al. [10, 11] firstly developed the cross missing rib (also called cross-chiral) model to describe the auxetic behavior in two dimensions of a honeycomb or foam-type material. Scarpa et al. [12] then evaluated the equivalent thermal conductivities of cross-chiral configurations by analytical closed-form solutions and Finite Element simulations. Lu et al. [13, 14] have investigated the elastic properties of 3D cross missing rib structures under uniaxial tension and compression. Farrugia et al. [15] carried out an extensive investigation via numerical simulations and experimental testing on the missing rib square grid structure, to clarify how the various geometric parameters affect the deformation mechanism of the grid itself.

Macroscopic auxetic cellular structures in the form of 2D re-entrant honeycombs were firstly suggested by Gibson et al. [16]. As a special form of re-entrant honeycomb, the mechanical behavior of composite star-shaped inclusions with a rotational symmetry of order 4 was numerically investigated by Theocaris et al. to show the influence of the microstructure geometry over the Poisson's ratio [17]. Grima et al. [18] assessed the potential for the auxetic behavior of a novel class of connected stars units with rotational symmetry of order 3, 4, 6 and explained the reasons for the presence or absence of a negative Poisson's ratio in these systems. The same Authors discussed how star or triangular shaped perforated sheets can be made to exhibit negative Poisson's ratio [19]. More recently, various star-shaped metamaterials have been investigated in terms of their specific equivalent mechanical behavior, band gap properties and impact energy absorption performance [20-27]. By introducing re-entrant core cells to the center of a basic chiral cell, Jiang et al. [8] have designed new hybrid chiral mechanical metamaterials with cell-opening mechanisms under very large range nonlinear geometric and materials strains. The Authors of the present paper have proposed a novel auxetic metamaterial configuration based on a re-entrant core and lateral ligaments, together with a cross missing rib grid of same dimensions as a benchmark. The new metamaterial exhibits a wider and tunable ranges of mechanical properties and larger in-plane deformations capabilities [28].

With modern additive manufacturing currently, the design and use of auxetic metamaterials for practical engineering applications has increased significantly. A circular plate made of star-shape auxetic joining plies has been proposed in [29]; its mechanical response has been simulated under normal pressure to obtain desired stiffness and a quasi-linear behavior without changing the structural geometry, materials or layout of the plate constituent elements. Ren et.al [30] designed, fabricated and experimentally evaluated the concept of auxetic nails, also providing a new critique for assessing the real advantages and limitations of auxetic materials and structures. Recently, a variety of auxetic metastructures have been developed. Some examples include anti-trichiral stents of equilateral triangle core [31], axisymmetric auxetic structures of re-entrant and double U configurations [32, 33], cylindrical NPR crash box of double-V unit cell [34], new spiral auxetic fiber structures [35]， auxetic bone screws [36] as well as the dome-shaped NPR cellular structures [37].

The present work describes a novel concept of hybrid auxetic metamaterial with a symmetric star-shape core unit cell and lateral missing ribs based on our previous work related to hybrid auxetic re-entrant metamaterials [28]. Taking the star configuration as a benchmark, we design hybrid auxetic metamaterial systems with different core unit cells (star-shape, cross-chiral with same dimensions as well as its special form of re-entrant) and constant type of connecting tessellation based on the missing rib model. The effects of the geometric parameters on in-plane elastic constants of the hybrid auxetic metamaterial system have been parametrically investigated via FEM to identify optimized RUCs along the x and y directions of a Cartesian frame. We then design two groups of metastructures with cylindric and cubic shapes made from the optimized RUCs. The macroscopic mechanical behavior of the two groups of metastructures under internal radial pressure have been simulated numerically. Finally, we have evaluated the influence of the number of optimized RUCs along the circumferential and axial directions on mechanical performances of two metastructures.

2. Methodology

2.1 Structure design

The novel hybrid star missing rib metamaterial is designed by taking a star-shape core unit cell with horizontal and vertical symmetry and lateral ligaments. This design is based on our previous re-entrant missing rib auxetic metamaterial [28]. The geometric features of a quarter RUC are defined as: (1) inclined wall lengths H and L, internal inclined angles φ and θ, internal thickness t_1 for the star core unit cell; (2) the length b_1 : b_4 and thickness t_1, t_2 for the internal and external ligaments, respectively (see Fig. 1 (a)). The out-plane thickness of one RUC is indicated as h_z and it is not shown in this paper. Three types of constraint geometry conditions for the

configuration need to be satisfied: (1) $\theta > 0^{\circ}$, $\varphi > 0^{\circ}$, $\theta < \frac{\pi}{2} - \varphi$, $H\cos\varphi - L\sin\theta - t_1/2\cos\theta > 0$, $L\cos\theta - H\sin\varphi - t_1/2\cos\varphi > 0$. These constraints are necessary to prevent self-contact of the core unit cell during small and large deformations. Another set of geometry constraints is (2) $b_1 > x_A$, $b_2 > y_A$, where x_A and y_A are the coordinates of intersection point A; those are to prevent contacts between the core unit cell and the external ribs along the x and y directions. An additional set of constraints is (3) $b_3 > b_1 + t_2$, $b_4 > b_2 + t_2$; those are put in place to evade the contacts between external ribs along the x and y directions. The geometry of the star missing rib RUC is defined by nondimensional parameters α , β and γ , where $\alpha = H/L$ is the inclined wall aspect ratio, $\beta = t_1/L$ is the thickness ratio of core unit cell and $\gamma = t_1/t_2$ is the thickness ratio of internal and external ribs. Moreover, the parameter c is introduced for setting the length between internal and external ribs: $b_1 = cx_A$, $b_2 = cy_A$, $b_3 = c \times (b_1 + t_2)$ and $b_4 = c \times (b_2 + t_2)$, where c is a constant greater than one. The new star missing rib RUC and the cross missing rib RUC with same dimensions are represented in Fig. 1 (b) and (c). In these figures the geometric parameters are $\alpha = 0.5$, $\beta = 0.1$, $\gamma = 0.5$, $c = 1.05$, $t_1 = 2$, $\varphi = 10^{\circ}$ and $\theta = 20^{\circ}$. Additionally, the star missing rib RUC can be changed into a re-entrant configurations when the angles φ or θ are equal to zero.

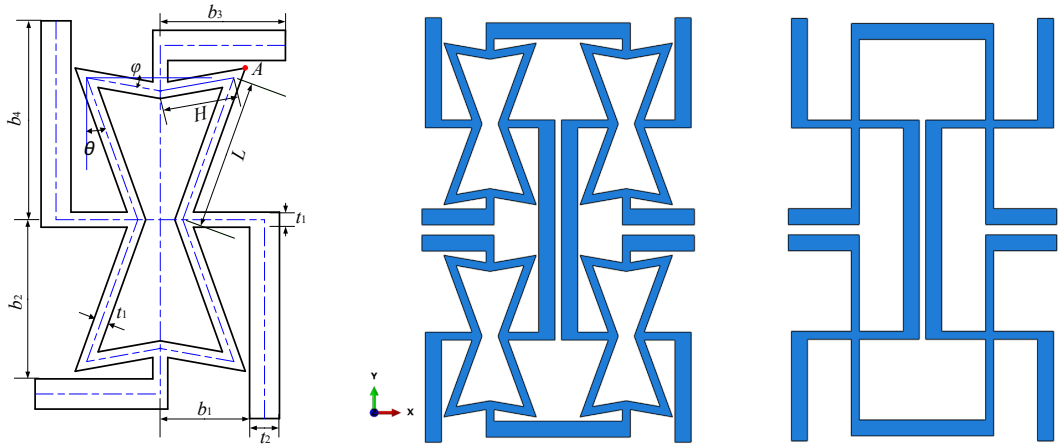

(a) **(b)** **(c)**

Figure 1. Design of the novel star missing rib metamaterial: (a) one quarter of RUC, (b) star missing rib RUC, (c) same-sized cross missing rib RUC.

A feasible geometry region enclosed by two angles φ and θ at different aspect ratios α and β can be identified according to the constraint inequalities described above (Fig. 2). The available range for the two angles is maximum when $\alpha = 1$. Because of the symmetry of the star shape, the variation of β with angle φ (or θ) under $\alpha = 0.5$ is the same as that of β with θ (or φ) when $\alpha = 2$. This indicates that the mathematical functions that describe these curves are mutually

inverse. In the following part of this paper we will therefore only examine the variations of the mechanical performance along the *i* direction ($i=1,2$) with φ (or θ) at $\alpha=0.5$ being the same as those calculated along the *j* direction ($j=2,1$) with θ (or φ) for $\alpha=2$.

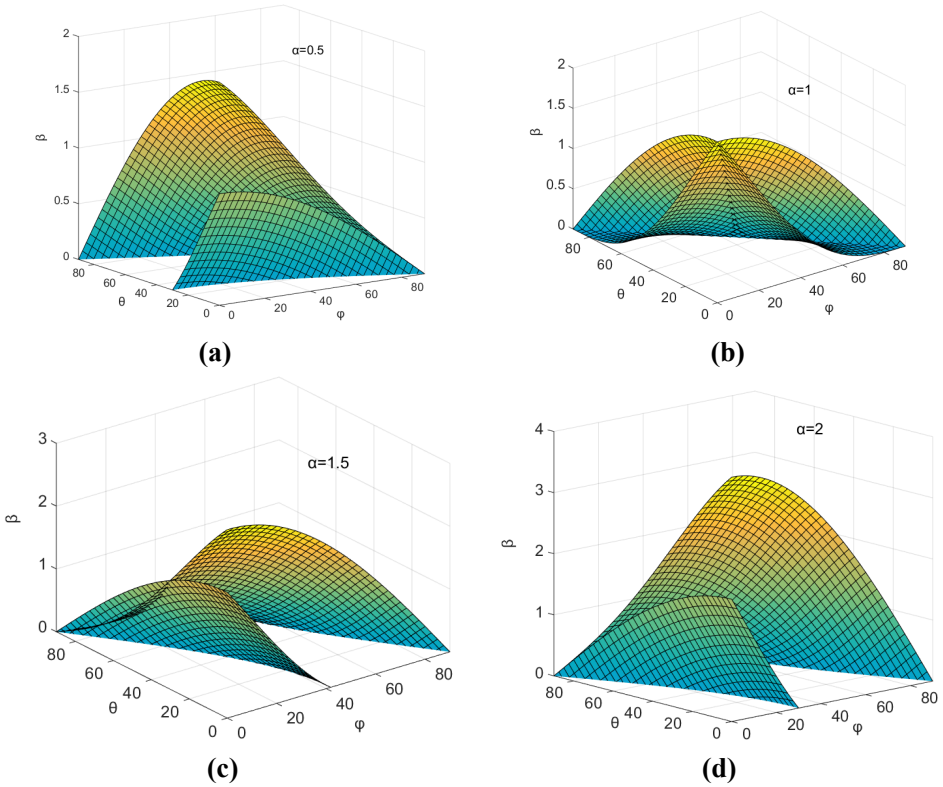

Figure 2. Aviable variation of inclined angle φ and θ with β of the star core unit cell when: (a) $\alpha=0.5$, (b) $\alpha=1$, (c) $\alpha=1.5$, (d) $\alpha=2$.

2.2 Relative density

The mechanical properties of auxetic metamaterials primarily depend on the relative density and the importance of this parameter exceeds those of others in lattice or porous materials [27]. The relative densities of a hybrid auxetic metamaterial system with different core unit cells and lateral missing ribs can be calculated by inspection as:

$$\rho_{\substack{star\\re\text{-}entrant}} = \frac{\rho^{*}_{\substack{star\\re-entrant}}}{\rho_s} = \frac{\beta\cos(\varphi+\theta)}{c^2}\times\frac{E\cos(\varphi+\theta)+c\beta\gamma(c+\gamma)(C+D)+F+G}{(A\cos(\varphi+\theta)+C\times c\beta\gamma)\times(B\cos(\varphi+\theta)+D\times c\beta\gamma)} \tag{1}$$

$$\rho_{cross} = \frac{\rho^{*}_{cross}}{\rho_s} = \frac{\beta\cos(\varphi+\theta)}{c^2}\times\frac{E\cos(\varphi+\theta)+c\beta\gamma(c+\gamma)(C+D)}{(A\cos(\varphi+\theta)+C\times c\beta\gamma)\times(B\cos(\varphi+\theta)+D\times c\beta\gamma)} \tag{2}$$

where $A=2c\gamma\cos\theta+2\beta$, $B=2c\gamma\alpha\cos\varphi+2\beta$, $C=\sin\varphi+\cos\theta$, $D=\cos\varphi+\sin\theta$,

$E=(A+B)\times(c+\gamma)-\beta(\gamma^2+2\gamma+2c)$,

$F=2\gamma^2(\alpha\sin\varphi-\alpha\cos\varphi+\sin\theta-\cos\theta+2\alpha+2)-2\gamma(\beta+2)+2c\beta$,

$G=-\beta\gamma^2\left(1+0.5\tan\theta+0.5\tan\varphi+\sec\theta+\sec\varphi\right)$.

Equations (2) show that the nondimensional parameters α, β, γ, the angles

θ, φ and the constant c all make an impact on the relative density of the hybrid auxetic metamaterial system.

2.3 Finite Element models

The finite element analysis is performed using the commercial software ABAQUS 6-14. The geometry of the numerical model is the same as the one shown in Fig. 1 (b). the core material has a Young's modulus $E_s = 2265\text{MPa}$ and Poisson's ratio $\upsilon = 0.25$ [28]. Models were meshed with C3D8R hex-dominated linear reduced brick elements with a mesh seed of $t_1/4$ to ensure accurate mesh convergence, especially on the sharp corners of the star RUC (Fig. 3 (a)). Fig. 3 (b) shows the resulting model with 103,648 elements. The uniaxial in-plane tension was simulated using periodic boundary conditions ($U_1 = UR_2 = UR_3 = 0$ and $U_2 = UR_1 = UR_3 = 0$) applied on the left and bottom edges of one RUC, and displacement $U_i = 1$ and $UR_3 = 0$ ($i = 1,2$) imposed on the right (or top) edges of RUC [38]. Biaxial loading was used to simulate pure shear with identical boundary conditions as above and displacements $U_1 = 1$, $U_2 = -1$ without in-plane rotation [39].

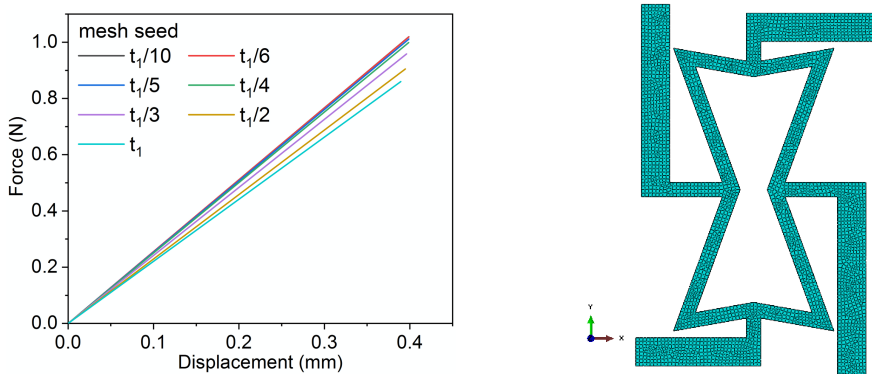

Figure 3. Mesh convergence analysis of the FE models: (a) force-displacement curves with different mesh seeds, (b) one quarter of meshing RUC

The effective in-plane moduli and the Poisson's ratios of one RUC are determined as [40]:

$$E_i = \frac{F_i L_i}{h_z L_j u_i}, \qquad G_{12} = \frac{F_i L_i - F_j L_j}{2h_z (u_i L_j - u_j L_i)}, \qquad \nu_{ij} = -\frac{u_j L_i}{u_i L_j} \tag{3}$$

Where F_i and F_j are the total reaction forces along the i, j directions on the prescribed boundary, L_i and L_j are the lengths of one RUC along the i and j directions ($i = 1,2$, $j = 2,1$), h_z is the out-plane thickness and u_i and u_j are the applied displacement along the i , j directions.

3. Parametric study and discussions

3.1 Unit cell optimization

Based on our previous study [28], then constant c (greater than one) is designed

to adjust the distance between the core unit cell and the external ligament, as well as of changing the length of the external ligament. It provides an important effect on both the design of the lattice and its mechanical properties. The value of c dictates a RUC shape that avoids the contact between the external ligament and the core unit cell and – at the same time – does not decrease the effect of the core unit cell on the mechanical performance. Therefore, the value of $c = 1.05$ is used in this section for the unit cell optimization.

It is known that the re-entrant shape is a special form of star structure with angle $\varphi = 0^{\circ}$. We can also observe from Fig. 2 that no mutual interaction between φ and θ occurs when $\alpha = 0.5$ and $\alpha = 2$. Therefore, the previous optimized results related to the re-entrant missing rib RUC ($\alpha = 2$, $\theta = 60^{\circ}$) for uniaxial loading along the x direction and $\alpha = 0.5$, $\theta = 0^{\circ}$ for uniaxial loading along the y direction and in-plane shear loading [28] remain valid for the present hybrid auxetic metamaterial system. These two optimized conditions above are abbreviated as Condition X and Condition Y. Fig. 1 also shows that the parameter φ is used to adjust the different shape of core unit cell in the hybrid auxetic metamaterial system. Its available ranges are shown in Fig. 2 (a) and Fig. 2 (d). The effect of the angle φ on mechanical behavior of the new hybrid metamaterial system can therefore be investigated within the range $0 \le \varphi \le 10^{\circ}$ for Condition X, and $0 \le \varphi \le 60^{\circ}$ for Condition Y. The hybrid metamaterial system related to Condition X is featured in Fig. 4, where the star missing rib RUC of $\varphi = 10^{\circ}$ in the middle represents an intermediary link to connect the left re-entrant missing rib RUC by changing φ, as well as to connect the right cross missing rib RUC with same dimensions. Similar considerations are valid for the hybrid metamaterial system of Condition Y in Fig. 5. The star missing rib RUC of the configuration at $\varphi = 60^{\circ}$ in Fig. 5 (b) becomes the optimized re-entrant missing rib RUC in Fig. 4 (a), with identical dimensions but different boundary conditions. It can be therefore concluded that the star missing rib RUC has a larger deformability compared to the one provided by the re-entrant configuration.

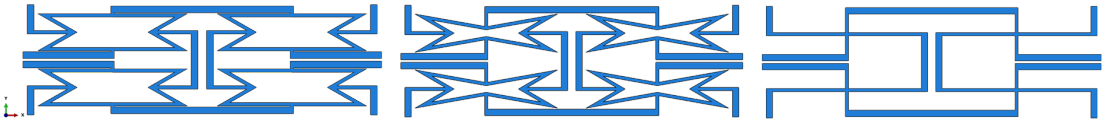

(a) **(b)** **(c)**

Figure 4. The hybrid metamaterial system related to Condition X with $\beta = 0.1$, $\gamma = 0.5$, $c = 1.05$, $t_1 = 2$: (a) optimized re-entrant RUC of $\varphi = 0^{\circ}$ [28], (b) new star RUC of $\varphi = 10^{\circ}$, (c) cross RUC of $\varphi = 10^{\circ}$ with same dimensions as the new star RUC.

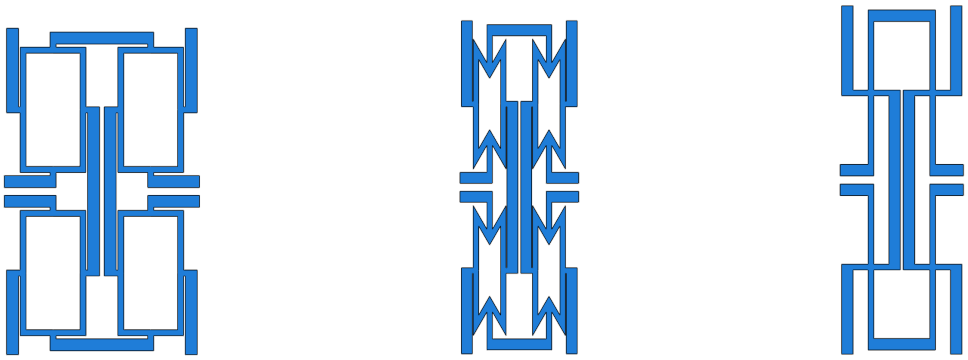

(a) **(b)** **(c)**

Figure 5. Hybrid metamaterial system related to Condition Y with $\beta = 0.1$, γ=0.5, $c = 1.05$, $t_1 = 2$: (a) optimized re-entrant RUC of $\varphi = 0^\circ$ [28], (b) new star RUC of $\varphi = 60^\circ$, (c) cross RUC of $\varphi = 60^\circ$ with same dimensions as the new star RUC.

3.2 The variation of the relative density

Comparisons of the relative density between three RUCs with variable γ have been carried out according to Eq. (1) (2) and the optimization described above (Fig.6). The relative density of the three RUCs all decline with increasing γ. The novel star missing rib RUC has a large relative density compared to those of the re-entrant and the cross RUCs under optimized conditions related to loading along the y direction and in-plane shear (Fig. 6 (a)). This leads to the decrease of the specific stiffness $\left(E_2^*/E_c\right)/\left(\rho/\rho_c\right)$, discussed later. The relative density of the re-entrant RUC optimized for loading along x direction for $\alpha = 1$, $\theta = 40^\circ$ is however always higher compared with those of the star and cross RUCs (Figs. 6 (b) and 6 (c)).

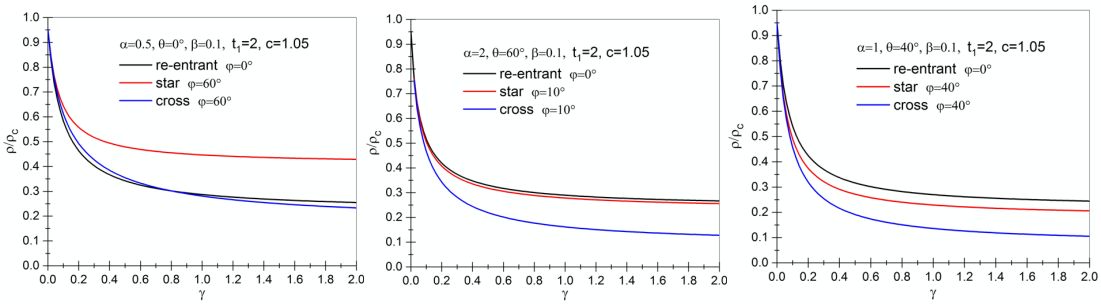

(a) **(b)** **(c)**

Figure 6. The variation of the relative density for the hybrid metamaterial system verse γ, when $\beta = 0.1$, $c = 1.05$, $t_1 = 2$ and : (a) Condition X, (b) Condition Y, (c) $\alpha = 1$, $\theta = 40^\circ$.

3.3 Parametric analysis

The variations of the in-plane mechanical behavior with thickness ratio γ based on the above parameter optimization results are shown in Fig. 7. Figs. 7 (a-d) indicate that the nondimensional moduli E_i^*/E_c and the specific stiffness $\left(E_i^*/E_c\right)/\left(\rho/\rho_c\right)$ $(i = 1,2)$ for the three RUCs have all a similar variation (first increase and then

decrease as γ increases). The star missing rib RUC exhibits the greatest non-dimensional Young's modulus E_1^*/E_c and E_2^*/E_c in the range of $\gamma \le 0.5$ and $\gamma > 0.5$, respectively (Figs. 7 (a) and 7 (b)). Additionally, the star missing rib RUC presents a larger specific stiffness $\left(E_1^*/E_c\right)/\left(\rho/\rho_c\right)$ (for $\gamma \le 0.5$) and a higher $\left(E_2^*/E_c\right)/\left(\rho/\rho_c\right)$ for the whole γ range compared with those of the re-entrant RUC. However, the specific stiffnesses $\left(E_i^*/E_c\right)/\left(\rho/\rho_c\right)$ ($i=1,2$) are lower than those of the cross RUC, and this can be explained by their high relative density (Figs. 7 (c) and 7 (d)). The effective Poisson's ratios υ_{12}^* and υ_{21}^* for the re-entrant and star missing rib RUCs both decrease with increasing γ (Figs. 7 (e) and 7 (f)). The Poisson's ratio υ_{12}^* of the cross RUC exhibits a trend of descent, gradual ascent and descent again, while its Poisson's ratio υ_{21}^* decreases when γ becomes large. In the three RUCs, the new star RUC exhibits a greater negative Poisson's ratio υ_{12}^* for $\gamma < 0.8$ and a superior auxetic behavior υ_{21}^* in the whole region of γ. This can be interpreted as the symmetric star core unit cell possessing a larger compliance compared with those of the cross-chiral and the re-entrant shapes. The nondimensional in-plane shear moduli G_{12}^*/E_c and $\left(G_{12}^*/E_c\right)/\left(\rho/\rho_c\right)$ all manifest a steadily rising trend with increasing γ (Figs. 7 (g) and 7 (h)). The star missing rib RUC provides the best shear performance, which can be ascribed to the presence of the middle star cell and the four joints between the cross ligaments being the main components to bear the loading in this configuration [28].

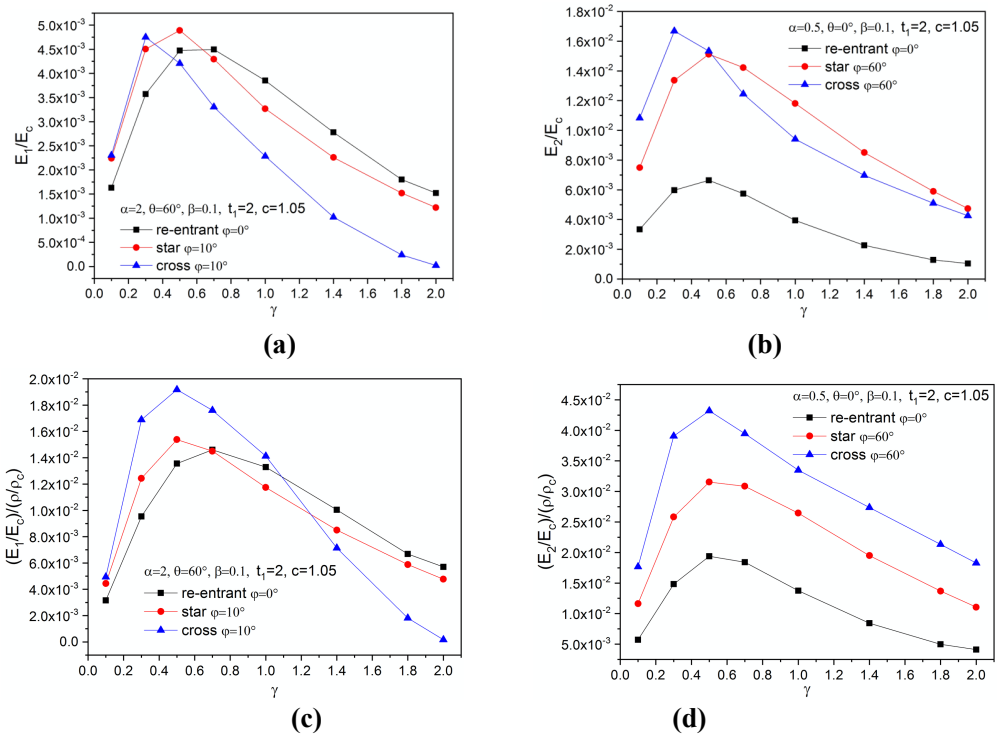

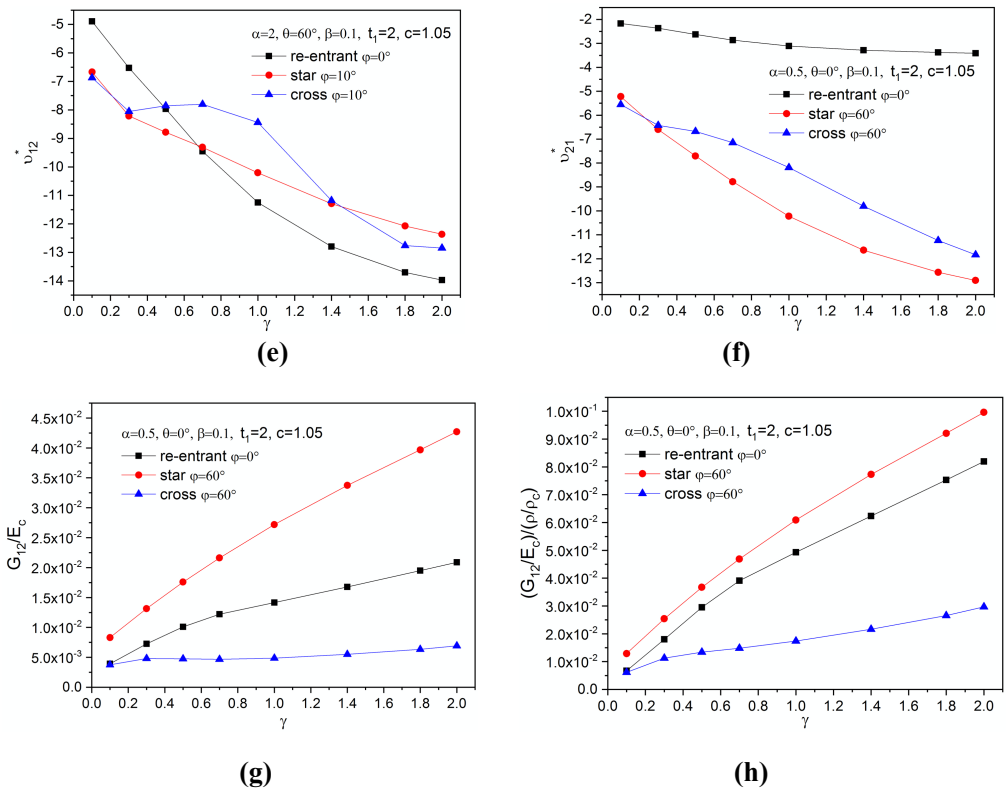

Figure 7. The effect of γ on in-plane mechanical property of the hybrid metamaterial system: (a) E_1^*/E_c, (b) E_2^*/E_c, (c) $\left(E_1^*/E_c\right)/\left(\rho/\rho_c\right)$, (d) $\left(E_2^*/E_c\right)/\left(\rho/\rho_c\right)$, (e) υ_{12}^*, (f) υ_{21}^*, (g) G_{12}^*/E_c, (h) $\left(G_{12}^*/E_c\right)/\left(\rho/\rho_c\right)$.

A further comparison of the mechanical properties for the hybrid auxetic metamaterial system in optimized Conditions X and Y are given in Table 1. In this case the parameters used are $\varphi=10^{\circ}$ (or $\varphi=60^{\circ}$) for the star and cross missing rib RUCs with same dimensions, $\varphi=0^{\circ}$ for the re-entrant missing rib RUC; the enhancement percentage is expressed here as: $\mathrm{EP_1}=(\text{star-reentrant})/\text{star}$ and $\mathrm{EP_2}=(\text{star-cross})/\text{star}$, respectively. The new star missing rib RUC along the *x* direction has a larger stiffness and NPR than those of its special form re-entrant and cross RUCs. The new star missing rib RUC under loading along the *y* direction manifests a greater auxetic behavior and better shear resistance compared with the other two RUCs. The stiffness E_2^*/E_c and specific stiffness $\left(E_i^*/E_c\right)/\left(\rho/\rho_c\right)$ $(i=1,2)$ for the star missing rib RUC are however 1.32% and 24.6%/ 37.14% lower than those of the cross RUC with same dimensions. This can be interpreted as a consequence of its complex configuration and larger relative density.

Table 1 Comparison of the in-plane mechanical behavior between the three missing rib RUCs when $\beta=0.1$, $\gamma=0.5$, $t_1=2$, $c=1.05$.

	Condition X with $\varphi=10^{\circ}$, $\varphi=0^{\circ}$			Condition Y with $\varphi=60^{\circ}$, $\varphi=0^{\circ}$				
	E_1^*/E_c	$\frac{E_1^*/E_c}{\rho/\rho_c}$	υ_{12}^*	E_2^*/E_c	$\frac{E_2^*/E_c}{\rho/\rho_c}$	υ_{21}^*	G_{12}^*/E_c	$\frac{G_{12}^*/E_c}{\rho/\rho_c}$
star	4.89×10^{-3}	1.54×10^{-2}	-8.785	1.51×10^{-2}	3.15×10^{-2}	-7.704	1.76×10^{-2}	3.67×10^{-2}
re-entrant	4.47×10^{-3}	1.36×10^{-2}	-7.963	6.64×10^{-3}	1.94×10^{-2}	-2.625	1.01×10^{-2}	2.95×10^{-2}
cross	4.21×10^{-3}	1.92×10^{-2}	-7.855	1.53×10^{-2}	4.32×10^{-2}	-6.677	4.75×10^{-3}	1.34×10^{-2}
EP_1	8.59%↑	11.69%↑	9.35%↑	56.03%↑	38.41%↑	65.92%↑	42.61%↑	19.62%↑
EP_2	13.91%↑	-24.68%↓	10.58%↑	-1.32%↓	-37.14%↓	13.33%↑	73.01%↑	63.49%↑

where enhancement percentage is $EP_1=(\text{star-reentrant})/\text{star}$, $EP_2=(\text{star-cross})/\text{star}$.

We then consider the variations of the mechanical properties versus the β taking, for example, the optimized Condition Y with parameters $\gamma=0.5$, $t_1=2$, $c=1.05$ with $\varphi=0^{\circ}$ and $\varphi=60^{\circ}$ applied to the re-entrant and the new star (or cross shape with same dimension) missing rib RUCs. Fig. 8 shows how the increase of the cell wall aspect ratio β leads to a sharp increase of E_2^*/E_c, which provides an interesting insight about the way to design the in-plane modulus by altering β [41]. For a fixed β, the novel star missing rib RUC has the largest nondimensional elastic modulus E_2^*/E_c and negative Poisson's ratio υ_{21}^* among the three RUCs (Fig. 8 (a) and 8 (b)). However, due to the impact of relative density, the star missing rib RUC has a lower specific stiffness $\left(E_2^*/E_c\right)/\left(\rho/\rho_c\right)$ compared with that of cross RUCs with same dimensions. That specific stiffness is however still larger than that of the re-entrant RUCs. Fig. 8 (c) shows that the star missing rib RUC has the most robust in-plane shear properties than the other two RUCs when $\beta=0.1$. Whereas, in the range of $\beta>0.2$, the re-entrant missing rib RUC provides the best shear performance of all. The shear stiffness of the star missing rib RUC is only superior to the one of a cross RUC.

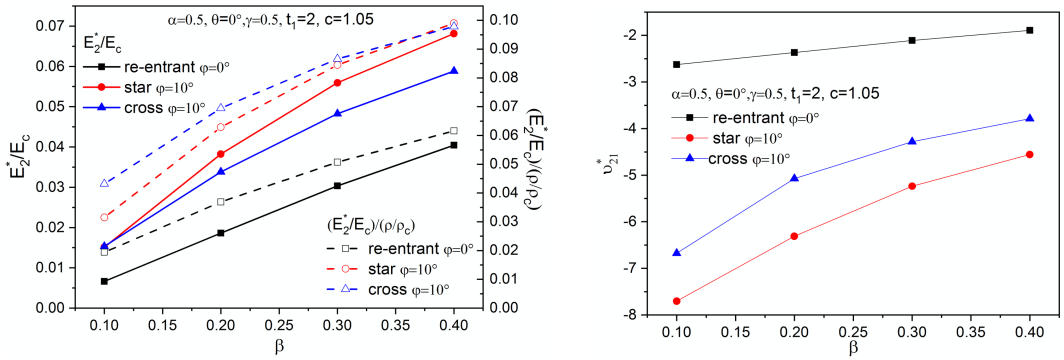

(a) **(b)**

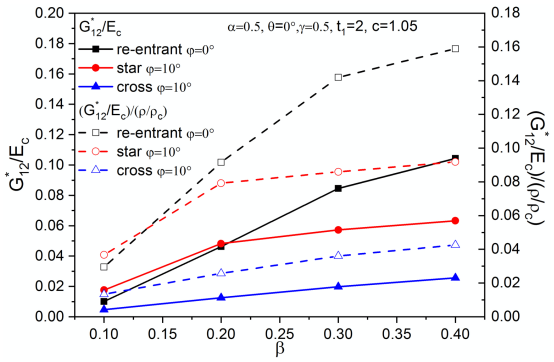

(c)

Figure 8. The effect of β on mechanical property of the hybrid metamaterial system under Condition Y with $\gamma = 0.5$, $t_1 = 2$, $c = 1.05$: (a) E_2^*/E_c and $\left(E_2^*/E_c\right)/\left(\rho/\rho_c\right)$, (b) υ_{21}^*, (c) G_{12}^*/E_c and $\left(G_{12}^*/E_c\right)/\left(\rho/\rho_c\right)$.

We can come to the conclusion that the new star missing rib RUC under specific sets of parameter conditions represents a combination of enhanced stiffness and greater auxetic behavior together. This provides a useful insight into the design, fabrication and analysis of auxetic metastructures.

4. Application of optimized RUCs

The analysis performed above shows that the star missing rib RUC provides enhanced elastic moduli and larger auxetic deformation compared to the other two configurations. We present in this section two groups of innovative auxetic metastructures with cylindrical and cubic shapes, which consist of the optimized star missing rib RUC along the *x* and *y* directions. The mechanical behaviors of the two groups of metastructures under inner radial pressure have been analyzed using finite elements. The influence of the structural design parameters on the effective mechanical properties of the metastructures has also been evaluated. The FE models used here are linear elastic, with the constituent material properties, element type and mesh convergence being the same as shown in Section 2.3. A uniform inner radial pressure $\sigma_r = 1\text{MP}a$ has been applied to the internal surface of the structures.

4.1 Design of the auxetic metastructures

Two groups of metastructures of cylindric and cubic shape with same dimensions have been designed on the basis of the optimized star missing rib RUC under Condition X with parameters $\varphi = 10^{\circ}$, $\beta = 0.1$, $\gamma = 0.5$, $t_1 = 8$, $c = 1.2$ (Fig. 9 (a)). The basic RUCs were arrayed along the *x* (length) and *y* (width) directions to generate a 3D structure, which was then rolled up axisymmetrically for 360 degrees (or by folding with 90 degrees) along the central axis to create a solid body for cylindrical (or cubic) metastructures [42]. The two metastructures have a longitudinal length

$L_y = N_L \times l_y$, a circumferential (or lateral) length along the central line $L_\theta = L_{xz} = N_c \times l_x$ as well as an out-plane thickness $h_z = 16\text{mm}$ (l_y and l_x are the height and length of one RUC, N_L and N_c are the numbers of optimized star RUCs along axial and circumferential directions - see Fig. 9 (a)). When $N_L = 4$ and $N_c = 2$, the overall dimensions of the metastructure of the optimized star RUC along the *x* direction are $352.58 \times 554.54 \times 16\text{mm}$ (Fig. 9 (a)). The optimized star missing rib RUC under Condition Y with parameters $\varphi = 60^\circ$, $\beta = 0.1$, $\gamma = 0.5$, $t_1 = 8$, $c = 1.2$ has been constructed in a similar manner. The overall dimensions of the two metastructures with $N_L = 4$ and $N_c = 2$ are $215.04 \times 311.79 \times 16\text{mm}$ (Fig. 9 (b)).

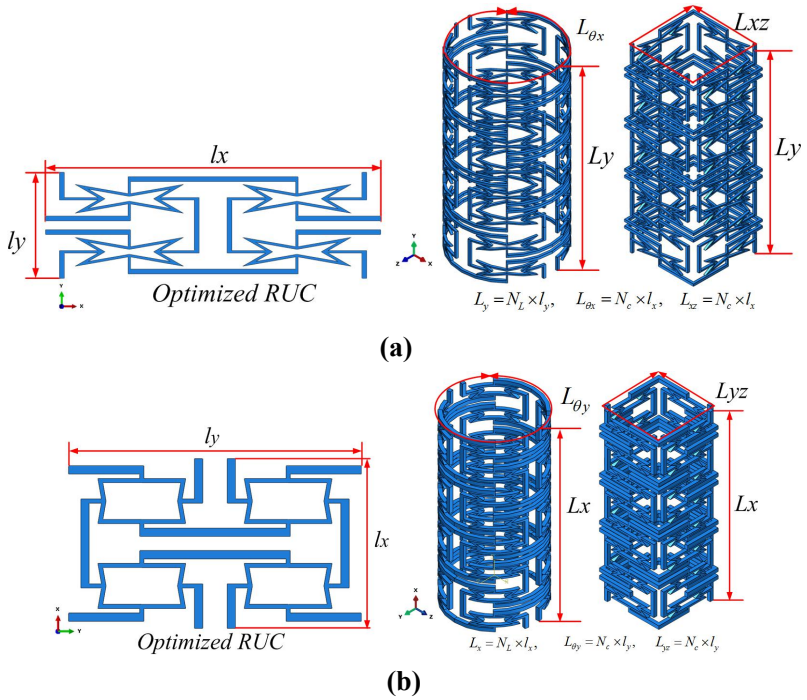

Figure 9. Two groups of metastructures with cylindric and cubic shapes, which consist of optimized star missing rib RUC: (a) along *x* direction, (b) along *y* direction, when $N_L = 4$ and $N_c = 2$.

4.2 The effect of the N_c parameter on the mechanical behavior of the metastructures

Two groups of metastructures with different numbers of optimized star RUCs along circumferential direction N_c have been scaled to identical dimensions, so that each layer includes 2, 4, 8, 16 RUCs. The slenderness ratio and the geometrical shape of the metastructures are kept constant. Accounting for the asymmetry along the *x*, *z* directions of a cubic tube, two groups of metastructures with $N_c = 2$ have been simulated full scale for one layer (Fig. 10 (a)). Boundary conditions of the type $U_i = 0$ ($i = 1,2,3$) have been imposed on the bottom *xz* plane of the structure, perpendicular to the longitudinal *y* axis. Due to the structural symmetry, a quarter of the two

metastructures with $N_c = 4,8$ (Fig. 10 (b) and Fig. 10 (c)) have been simulated with periodic boundary conditions $U_i = UR_j = UR_k = 0$ ($i, j, k = 1,2,3$ and $i \neq j \neq k$) along the *x*, *y* and *z* directions and applied on the correspondent degrees of freedom (DOFs) of the node pairs at the opposite plane (front and back, left and right, top and bottom) [43, 44].

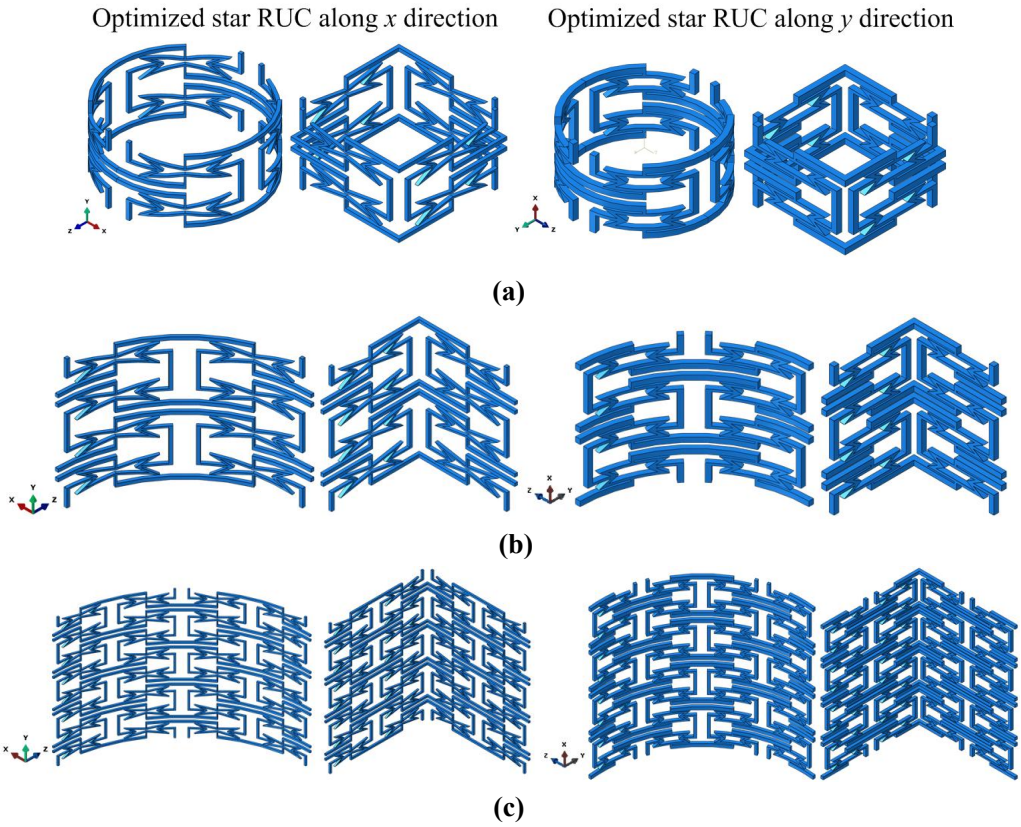

Figure 10. Two groups of metastructures with different numbers of optimized RUCs along the circumference: (a) $N_c = 2$, (b) $N_c = 4$, (c) $N_c = 8$. The metastructures are composed by the optimized star RUC along the *x* and *y* directions.

The elastic fields of the two groups of the metastructures with the optimized RUC along the *x* and *y* directions and $N_c = 2$ are shown in Fig. 11 and Fig.12, respectively. The longitudinal displacements along the *z* (or *y*) direction increase under radial inner pressure. This also happens for the radial (or transverse) displacements in the cases of the cylindric (or cubic) metastructures. There is evidence of an apparent NPR effect observed in Fig. 11 (a, b) and Fig. 12 (a, b), where the black and coloured contours are related to the undeformed and deformed structures, respectively. The elastic stress fields of the two metastructures are displayed in Fig. 11 (c) and Fig. 12 (c). The Von Mises stresses of the cylindric metastructure with optimized RUC along the *x* (or *y*) direction is respectively 40% and 27% lower than that of the cubic one. In addition, the Mises stress of the cylindric metastructure with optimized RUC along *y* direction is three times smaller than that of the optimized RUC along the *x* direction, clearly indicating a larger load capacity.

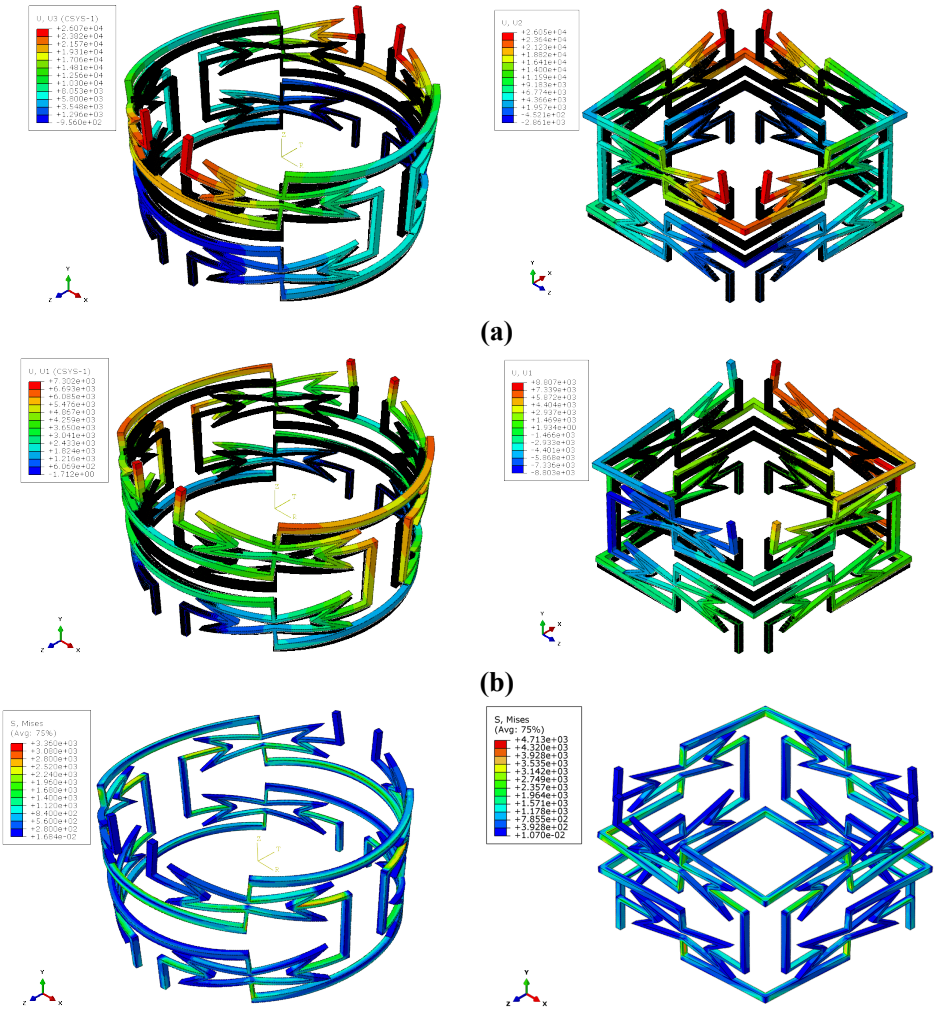

Figure 11. Elastic fields of the two metastructures with optimized RUC in *x* direction, when $N_c = 2$: (a) axial displacements, (b) radial (or transverse) displacements, (c) Von Mises stress.

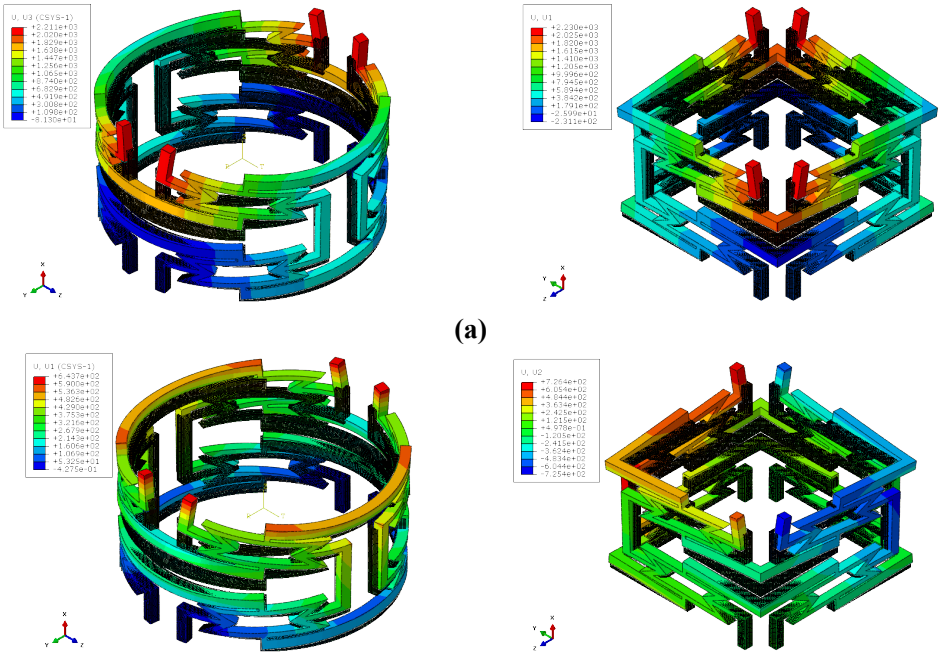

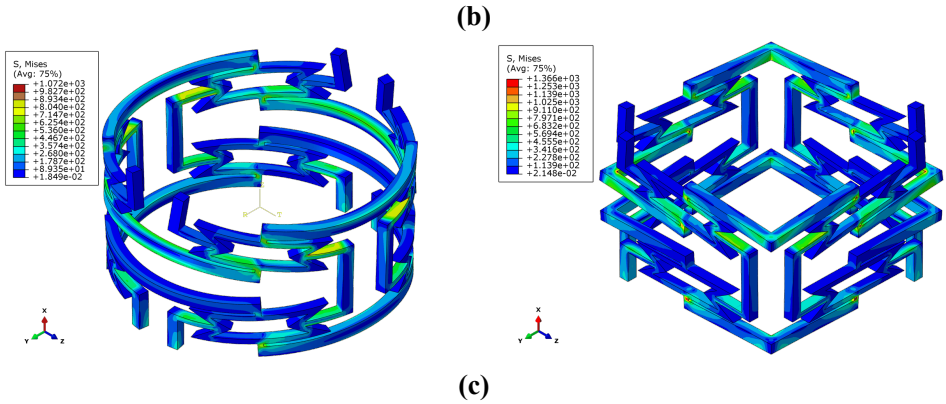

Figure 12. Elastic fields of the two metastructures with optimized RUC in *y* direction, when $N_c = 2$: (a) axial displacements, (b) radial (or transverse) displacements, (c) Von Mises stress.

Displacements along the longitudinal and radial (or transverse) directions of cylindric (or cubic) metastructures consisting of optimized RUC along the x and y directions with different numbers of N_c are listed in Table 2. Within the table U_i ($i = 1,2$) are the transverse (or longitudinal) and longitudinal (or transverse) displacements of the cubic metastructure composed by the optimized RUC along the x (or y) directions, U_z and U_r are the longitudinal and radial displacements of the cylindric metastructure.

Table 2 Displacements of the two groups of metastructures with different numbers of N_c along the circumferential direction.

Number of cells	Optimized star RUC in x direction				Optimized star RUC in y direction			
N_c	U_z	U_r	U_2	U_1	U_z	U_r	U_1	U_2
2	25535.5	7302	25456.5	8805	2131.62	643.7	2135.55	725.9
4	43704.1	9118	30638.1	13800	3425.13	722.6	2775.43	1223
8	66130	11640	51603.5	131600	6070.87	1077	4800.89	8700
16	130386	20870	102640	1053000	12093	1938	9479.06	65350

Under internal radial pressure of $\sigma_r = 1\text{MPa}$, the radial (or transverse) strain and the longitudinal strain for two groups of metastructures can be expressed as [45]:

$$\varepsilon_r = \frac{D_{final} - D_{initial}}{D_{initial}} \times 100\%, \quad \varepsilon_i = \frac{L_i^{final} - L_i^{initial}}{L_i^{initial}} \times 100\% \ (i = x, y), \quad \varepsilon_L = \frac{L_{final} - L_{initial}}{L_{initial}} \times 100\% \tag{6}$$

Where the subscript $i = x, y$ is the optimized RUC along the x and y direction, respectively.

The Poisson's ratio for two groups of metastructures with the optimized star missing rib RUC along the x and y directions can be written as:

$$\nu_{cylindric} = -\frac{\varepsilon_L}{\varepsilon_r}, \qquad \nu_{cubic} = -\frac{\varepsilon_L}{\varepsilon_i} \ (i = x, y) \tag{7}$$

The variations of the Poisson's ratio and Von Mises stress for two groups of metastructures with different N_c numbers are displayed in Fig. 13. From Fig. 13 (a), it can be observed that the Poisson's ratio of cylindric metastructures declines with

increasing N_c, showing a consistency with the results presented in [45, 46]. In addition, the cylindric metastructure of the optimized RUC in the *y* direction has a greater NPR than the one shown by the optimized RUC along the *x* direction. However, the variation of the Poisson's ratio for the cubic metastructure with N_c is just opposite and little difference in terms of Poisson's ratio exists between cubic metastructures made from optimized RUCs along the *x* and *y* directions. Fig. 13 (a) also shows that the auxetic deformation of the cylindric metastructure is much larger than the one provided by the cubic one. Fig. 13 (b) indicates that the von Mises stresses for the two groups of metastructures increase for an increase of the number of units N_c. When $N_c = 16$, the stress of the cylindric metastructure is ten times lower than the one provided by the cubic configuration; this is another clear indication of superior loading capacity.

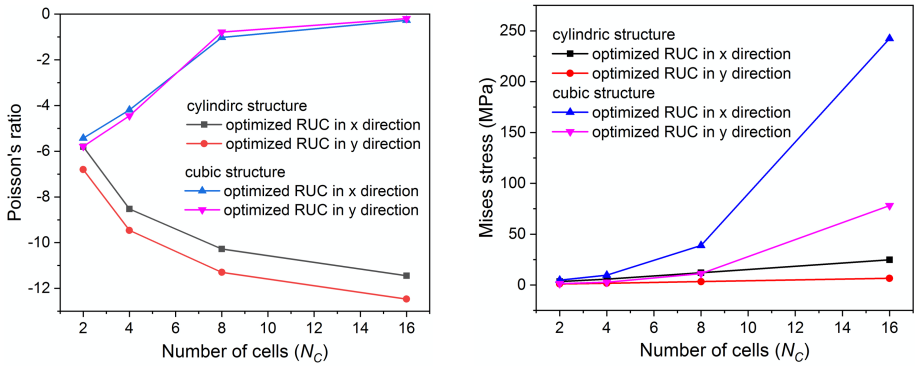

(a) **(b)**

Figure 13. The variations of Poisson's ratio (a) and Mises stress (b) for two groups of metastructures with different numbers of N_c along circumferential direction.

4.3 The effect of the parameter N_L on the mechanical behavior of metastructures

The influence of the number of optimized star RUCs along the longitudinal direction N_L on the two groups of metastructures with $N_c = 2$ has also been evaluated. The corresponding geometric dimensions and results of displacements for the metastructures are listed in Table 3. The effects of the parameter N_L on the Poisson's ratio and Von Mises stress fare shown in Fig. 14. The Poisson's ratio of the two metastructures increases with increasing N_L, similarly with the results shown in [45]. The auxetic behavior of the cylindrical metastructure is more distinct than that of the cubic assembly with the same dimensions. Moreover, the negative Poisson's ratio effect of the cylindrical metastructure with the optimized star RUC along the *y* direction is larger than the one of same structure with the optimized RUC along the *x* direction. As shown in Fig. 14 (b), the von Mises stress of the two metastructures almost remains constant with increased values of N_L. The stress of two metastructures with the RUC along the *x* direction is again approximately three times

larger than the one of the metastructure with the RUC along the y direction. Furthermore, the cylindric metastructure shows an enhanced stiffness, compared with the one of the cubic one.

Table 3 Geometric dimensions and displacements of the two groups of metastructures with different numbers of N_L along the longitudinal direction.

N_L	Optimized star RUC in x direction					Optimized star RUC in y direction				
	L_y	U_z	U_r	U_2	U_1	L_x	U_z	U_r	U_1	U_2
1	352.58	25535.5	7302	25456.5	8805	215.04	2131.62	643.7	2135.55	725.9
2	705.16	45630.2	7337	45540.7	8888	430.08	3893.75	629.5	3912.07	747.5
3	1057.74	66086.1	7373	65932.3	8955	645.12	5692.32	634.1	5706.27	749.1
4	1410.32	86190.4	7403	86428.3	8932	860.16	7486.93	635.6	7499.25	750

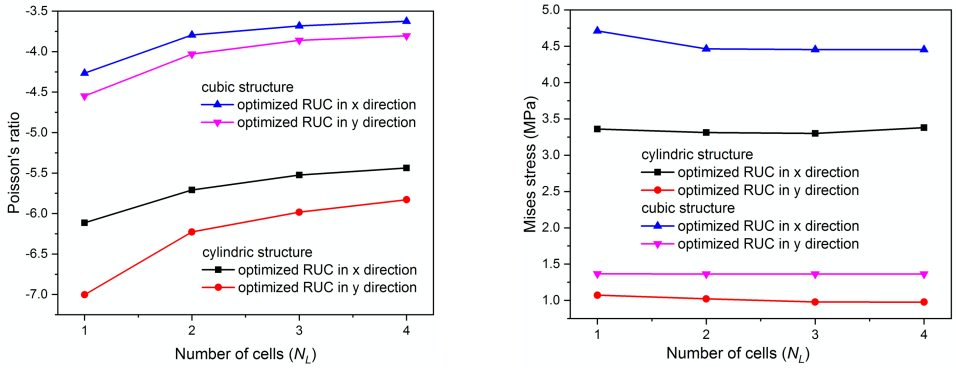

(a) **(b)**

Figure 14. The variations of Poisson's ratio (a) and Mises stress (b) for two groups of metastructures with different numbers of N_L along longitudinal direction.

One can clearly observe that the number of the optimized star RUCs along the circumferential direction has a larger impact on the macroscopic mechanical response of the auxetic metastructure than the one along the longitudinal direction, which is in accordance with the results shown in [45, 46]. The cylindrical metastructure made of the optimized RUC along the y direction exhibits in general both excellent stiffness values and a large auxetic behavior with increasing N_c and decreasing N_L values.

The versatility of the novel hybrid auxetic metamaterial with the star core unit cell and lateral ligaments provides potential broad ranges of practical applications. These new designs can be used to develop new material systems, sensors and actuators. In biomedical engineering, for instance, the new metamaterial can be used for stents, drug delivery and skin grafts due to its superior auxetic mechanical properties under large deformations [8, 23]. In view of the combination of high stiffness and NPR behavior, the novel star missing rib metamaterial could be suitable for applications in morphing wings and satellite antenna components [47, 48]. In addition, the configuration could be used in structures under severe temperature variations for possible dimensional stability and thermal expansion compensation. Furthermore, it should be noticed that the difficulty of manufacturing hinges and the stress concentrations induced by the star-sharp corners are still problems to be solved.

To overcome those issues, methods like filleting the critical points of the sharp edge [49] as well as introducing smoothing petal-shaped to replace the hinges [50] could be considered.

5. Conclusions

In this paper, a hybrid auxetic metamaterial system consisting of different core unit cells and lateral missing ribs has been proposed, in which the symmetric star shape was a benchmark to connect the cross-chiral configuration with same dimension as well as its special form of re-entrant shape. In-plane mechanical properties of the hybrid metamaterial system have been parametrically investigated and compared by finite element analysis to acquire the optimal RUC. It has been found that the optimized star missing rib RUC with parameters $\alpha = 2$, $\theta = 60^{\circ}$, $\varphi = 10^{\circ}$, $\gamma \le 0.5$ possess a stronger tension along x direction than other two RUCs. Meanwhile, the optimized star missing rib RUC with parameters $\alpha = 0.5$, $\theta = 0^{\circ}$, $\varphi = 60^{\circ}$, $\gamma \ge 0.5$ exhibits a better mechanical behavior in tension along the y direction as well as for planar shear, compared to the other two RUCs. Two classes of metastructures with cylindrical and cubic shapes under internal radial pressure have been then constructed and numerically simulated, on the basis of the aforementioned optimized star missing rib RUCs. The effects of the number of optimized RUCs along the circumferential and axial directions on the mechanical performance of the two groups of metastructures has been also analyzed. The proposed cylindric metastructure made of optimized star RUCs along the y direction exhibits a stronger load capacity and remarkable radial auxeticity when the number of RUCs along the circumferential direction is increased and the other design parameters are kept constant.

Declaration of conflicting interests

The author(s) declared no potential conflicts of interest with respect to the research, authorship, and/or publication of this article.

ORCID iD

Wenjiao Zhang ORCID iD https://orcid.org/0000-0003-2273-4569

References

1. Lakes R. Foam structures with a negative Poisson's ratio. Science 1987; 235: 1038–40.
2. Hou X, Silberschmidt VV. Metamaterials with negative Poisson's ratio: a review of mechanical properties and deformation mechanisms. Mechanics of advanced materials. New York: Springer; 2015.
3. Hong Hu, Minglonghai Zhang, Yanping Liu. Auxetic structures and mechanisms. Auxetic Textiles, The Textile Institute Book Series, 2019, Pages 19-56

4. X.L. Yu, J. Zhou, H.Y. Liang, Z.Y. Jiang, L.L.Wu. Mechanical metamaterials associated with stiffness, rigidity and compressibility: a brief review, Prog. Mater. Sci. 94 (2018) 114-173.
5. Alderson A, Alderson K, Attard D, Evans K, Gatt R, Grima J, et al. Elastic constants of 3-, 4-and 6-connected chiral and anti-chiral honeycombs subject to uniaxial in-plane loading. Compos Sci Technol 2010;70(7):1042-8.
6. Alderson A, Alderson K, Chirima G, Ravirala N, Zied K. The in-plane linear elastic constants and out-of-plane bending of 3-coordinated ligament and cylinder-ligament honeycombs. Compos Sci Technol 2010;70(7):1034-41.
7. Jerzy Smardzewski, Robert Kłos, Beata Fabisiak. Design of small auxetic springs for furniture. Materials and Design 51 (2013) 723–728.
8. Jiang, Yunyao, Li, Yaning. 3D Printed Auxetic Mechanical Metamaterial with Chiral Cells and Re-entrant Cores. Scientific Reports, 2018, 8: 2397.
9. Wenwang Wu, Wenxia Hu, Guian Qian, Haitao Liao, Xiaoying Xu, Filippo Berto. Mechanical design and multifunctional applications of chiral mechanical metamaterials: A review. Materials and Design 180 (2019) 107950.
10. C.W Smith, J.N Grima，K.E Evans. A novel mechanism for generating auxetic behaviour in reticulated foams: missing rib foam model. Acta mater. 48 (2000) 4349–4356.
11. Gaspar, N., Ren, X. J., Smith, C. W., Grima, J. N., & Evans, K. E. Novel honeycombs with auxetic behaviour. Acta Materialia, 53(8), (2005). 2439-2445.
12. L.Boldrin, F.Scarpa, R.Rajasekaran. Thermal conductivities of iso-volume centre-symmetric honeycombs, Composite Structures, 113, 498-506, 2014.
13. Z. Lu, Q. Wang, X. Li, Z. Yang, Elastic properties of two novel auxetic 3D cellular structures, Int. J. Solids Struct. 124 (2017) 46-56.
14. Qingsong Wang, Zhenyu Yang, Zixing Lu, Xiang Li. Mechanical responses of 3D cross-chiral auxetic materials under uniaxial compression. Materials & Design 186 (2020) 108226.
15. Pierre-Sandre Farrugia, Ruben Gatt, Enrico Zammit Lonardelli, Joseph N. Grima, Ken E. Evans. Different Deformation Mechanisms Leading to Auxetic Behavior Exhibited by Missing Rib Square Grid Structures. Phys. Status Solidi B, 2018, 1800186.
16. Gibson L.J., Ashby M.F., Schajer G.S., Robertson C.I.. The mechanics of two-dimensional cellular materials. Proc. R. Soc. London. A382 (1982).
17. Theocaris PS, Stavroulakis GE, Panagiotopoulos PD. Negative Poisson's ratios in composites with star-shaped inclusions: a numerical homogenization approach. Arch Appl Mech 1997; 67(4): 274-286.
18. J.N. Grima, R. Gatt, A. Alderson, K. Evans, On the potential of connected stars as auxetic systems, Mol. Simul. 31 (13) (2005) 925–935.
19. Joseph N. Grima, Ruben Gatt, Brian Ellul, Elaine Chetcuti. Auxetic behaviour in non-crystalline materials having star or triangular shaped perforations. Journal of Non-Crystalline Solids 356 (2010) 1980–1987.
20. Meng J, Deng Z, Zhang K, Xu X, Wen F. Band gap analysis of star-shaped honeycombs with varied Poisson's ratio. Smart Mater Struct 2015; 24(9): 95011.
21. Xiaobo Gong, Jian Huang, Fabrizio Scarpa, Yanju Liu, Jinsong Leng. Zero Poisson’s ratio cellular structure for two-dimensional morphing applications. Composite Structures 134 (2015) 384–392.
22. V. Carneiro, H. Puga, J. Meireles, Analysis of the geometrical dependence of auxetic

behavior in reentrant structures by finite elements, Acta Mech. Sinica 32 (2) (2016) 295–300.
23. Luke Mizzi, E.M. Mahdi, Kirill Titov, Ruben Gatt, Daphne Attard, Kenneth E. Evans, Joseph N. Grima, Jin-Chong Tan. Mechanical metamaterials with star-shaped pores exhibiting negative and zero Poisson's ratio. Materials and Design 146 (2018) 28–37.
24. Wenjiao Zhang, Shuyuan Zhao, Rujie Sun, Fabrizio Scarpa, Jinwu Wang. In-Plane Mechanical Behavior of a New Star-Re-Entrant Hierarchical Metamaterial. Polymers 2019, 11 (7), 1132.
25. Huan Wang, Zixing Lu, Zhenyu Yang, Xiang Li. A novel re-entrant auxetic honeycomb with enhanced in-plane impact resistance. Composite Structures 208 (2019) 758–770.
26. H. Wang, Z. Lu, Z. Yang, et al., In-plane dynamic crushing behaviors of a novel auxetic honeycomb with two plateau stress regions, Int. J. Mech. Sci. 151 (2019), 746–759
27. Lulu Wei, Xuan Zhao, Qiang Yu, Guohua Zhu. A novel star auxetic honeycomb with enhanced in-plane crushing strength. Thin-Walled Structures 149 (2020) 106623.
28. Wenjiao Zhang, Shuyuan Zhao, Fabrizio Scarpa, Jinwu Wang, Rujie Sun. In-plane mechanical behavior of novel auxetic hybrid metamaterials. Thin–Walled Structures 159 (2021) 107191.
29. R. Brighenti. Smart behavior of layered plates through the use of auxetic materials. Thin-Walled Structures 84 (2014) 432–442.
30. Xin Ren, Jianhu Shen, Phuong Tran, Tuan Duc Ngo, Yi Min Xie. Auxetic nail: Design and experimental study. Composite Structures 184 (2018) 288–298.
31. Ramin Hamzehei, Saeed Rezaei, Javad Kadkhodapour, Ali Pourkamali Anaraki, Alireza Mahmoudi. 2D triangular anti-trichiral structures and auxetic stents with symmetric shrinkage behavior and high energy absorption. Mechanics of Materials 142 (2020) 103291.
32. V.H. Carneiro, H. Puga. Axisymmetric auxetics. Composite Structures 204 (2018) 438-444.
33. Hang Yang, Li Ma. Design and characterization of axisymmetric auxetic metamaterials. Composite Structures 249 (2020) 112560.
34. Qiang Gao, Xuan Zhao, Chenzhi Wang, Liangmo Wang, Zhengdong Ma. Multi-objective crashworthiness optimization for an auxetic cylindrical structure under axial impact loading. Materials and Design 143 (2018) 120–130.
35. Qian Ma, Larry D. Peel. Development of spiral auxetic structures. Composite Structures 192 (2018) 310–316.
36. Yan Yao, Lizhen Wang, Jian Li, Shan Tian, Ming Zhang, Yubo Fan. A novel auxetic structure based bone screw design: Tensile mechanical characterization and pullout fixation strength evaluation. Materials and Design 188 (2020) 108424.
37. Nathanael Easey, Dmytro Chuprynyuk, W. M. Syazwan Wan Musa, Angus Bangs, Yousef Dobah, Anton Shterenlikht, Fabrizio Scarpa. Dome-Shape Auxetic Cellular Metamaterials: Manufacturing, Modeling, and Testing. Frontiers in Materials, 2019, 6:86.
38. K. Li, X.-L. Gao, G. Subhash. Effects of cell shape and cell wall thickness variations on the elastic properties of two-dimensional cellular solids. International Journal of Solids and Structures 42 (2005) 1777–1795.
39. Victor Salit, Tanchum Weller. On the feasibility of introducing auxetic behavior into thin-walled structures. Acta Materialia 57 (2009) 125–135.
40. Wenjiao Zhang, Robin Neville, Dayi Zhang, Fabrizio Scarpa, Lifeng Wang, Roderic Lakes. The two-dimensional elasticity of a chiral hinge lattice metamaterial. International Journal of Solids and Structures, 2018, 141-142: 254-263.

41. Jian Huang, Xiaobo Gong, Qiuhua Zhang, Fabrizio Scarp, Yanju Liu, Jinsong Leng. In-plane mechanics of a novel zero Poisson's ratio honeycomb core. Composites Part B 89 (2016) 67-76.
42. Chao Ma, Hongshuai Lei, Jun Liang, Wenwang Wu, TiejunWang, Daining Fang. Macroscopic mechanical response of chiral-type cylindrical metastructures under axial compression loading. Materials and Design 158 (2018) 198-212.
43. L. Ai, X.-L. Gao. Three-dimensional metamaterials with a negative Poisson's ratio and a non-positive coefficient of thermal expansion. International Journal of Mechanical Sciences 135 (2018) 101-113.
44. Xin-Tao Wang, Bing Wang, Xiao-Wen Li, Li Ma. Mechanical properties of 3D re-entrant auxetic cellular structures. International Journal of Mechanical Sciences 131-132 (2017) 396-407.
45. Wenwang Wu, Xiaoke Song, Jun Liang, Re Xia, Guian Qian, Daining Fang. Mechanical properties of anti-tetrachiral auxetic stents. Composite Structures 185 (2018) 381–392.
46. Xiao Li Ruan, Jie Jie Li, Xiao Ke Song, Hong Jian Zhou, Wei Xing Yuan, Wen Wang Wu, Re Xia. Mechanical Design of Antichiral-Reentrant Hybrid Intravascular Stent. International Journal of Applied Mechanics, 2018, 10 (10): 1850105.
47. A. Spadoni, M. Ruzzene, J. Static Aeroelastic Response of Chiral-core Airfoils. Intell. Mater. Syst. Struct. 18 (2007) 1067–1075.
48. S.Jacobs, C. Coconnier, D.DiMaio, F.Scarpa, M.Toso, J.Martinez. Deployable auxetic shape memory alloy cellular antenna demonstrator: design, manufacturing and modal testing. SmartMater. Struct. 21 (2012), 075013.
49. Kusum Meena, Sarat Singamneni. The role of filleting on the stressed state of a square grid auxetic structure. Procedia Manufacturing 30 (2019) 650–657.
50. Zhen-Pei Wang, Leong Hien Poh, Justin Dirrenberger, Yilin Zhu, Samuel Forest. Isogeometric shape optimization of smoothed petal auxetic structures via computational periodic homogenization. Comput. Methods Appl. Mech. Engrg. 323 (2017) 250–271.